



# CHORUS

This is the accepted manuscript made available via CHORUS. The article has been published as:

## Anchoring effect of distorted octahedra on the stability and strength of platinum metal pernitrides

Z. H. Fu, T. G. Bi, S. H. Zhang, S. Chen, E. Zurek, D. Legut, T. C. Germann, T. Lookman,  
and R. F. Zhang

Phys. Rev. Materials **3**, 013603 — Published 8 January 2019

DOI: [10.1103/PhysRevMaterials.3.013603](https://doi.org/10.1103/PhysRevMaterials.3.013603)

# **Anchoring Effect of Distorted Octahedra on the Stability and Strength of Platinum Metal Pernitrides**

Z. H. Fu,<sup>1,2</sup> T. G. Bi,<sup>3</sup> S. H. Zhang,<sup>1,2</sup> S. Chen,<sup>1,2</sup> E. Zurek,<sup>3</sup> D. Legut,<sup>4</sup> T. C. Germann,<sup>5</sup> T.  
Lookman,<sup>5</sup> and R. F. Zhang<sup>1,2,\*</sup>

<sup>1</sup>*School of Materials Science and Engineering, Beihang University, Beijing 100191, P. R. China*

<sup>2</sup>*Center for Integrated Computational Materials Engineering (International Research Institute for Multidisciplinary Science) and Key Laboratory of High-Temperature Structural Materials & Coatings Technology (Ministry of Industry and Information Technology), Beihang University, Beijing 100191, P. R. China*

<sup>3</sup>*Department of Chemistry, State University of New York at Buffalo, Buffalo, NY 14260-3000, USA*

<sup>4</sup>*IT4Innovations & Nanotechnology Centre, VSB-Technical University of Ostrava, CZ-70833 Ostrava, Czech Republic*

<sup>5</sup>*Theoretical division, Los Alamos National Laboratory, Los Alamos, New Mexico 87545, USA*

\*: Correspondence and requests for materials should be addressed to R.F.Z. (e-mail: [zrf@buaa.edu.cn](mailto:zrf@buaa.edu.cn))

## **Abstract**

The successful preparation of platinum metal pernitrides ( $\text{PmN}_2$ ) in high-temperature and high-pressure experiments has aroused great scientific interest, since it has long been thought that these systems could not be prepared, and also because of their intriguing mechanical properties. Although it is now widely recognized that  $\text{PmN}_2$  phases can be stabilized under high-pressure, the physical origin explaining their stability remains unknown. By means of high-throughput first-principles schemes, we reveal for the first time that the choice of specific space group of these pernitrides at high pressure can be quantified by the anchoring effect of distorted  $\text{PmN}_6$  octahedra. The competition between baddeleyite and marcasite is attributed uniquely to Pm dimerization, resulting in a profound enhancement of Pm-Pm bonding and N-N  $\pi$  antibonding, while Pm-N bonding plays a secondary role. The observed mechanical strength and atomic deformation mechanism of  $\text{PmN}_2$  suggest that they are ultra-incompressible yet soft. This is attributed to the breaking of elongated Pm-N bonds in the  $\text{PmN}_6$  octahedra, which is accompanied by a continuous semiconductor-semimetal-metal transition for the semiconducting  $\text{PmN}_2$  during straining. These findings shed light on the physical origin of high-pressure stabilization and highlight the importance of exploring deformation mechanisms in designing novel strong solids.

## I. INTRODUCTION

It was long believed that the platinum-metal (Pm) elements (i.e., Pt, Ir, Os, Pd, Rh, Ru) are unable to form stable compounds with nitrogen at ambient conditions, but their pernitrides ( $\text{PmN}_2$ ) have now been successfully synthesized under high pressure and high temperature [1-4]. By now experiments and theory have reached a consensus concerning the observed crystal structures and stoichiometry of  $\text{PmN}_2$  [5-8].  $\text{PtN}_2$  forms the pyrite structure, which is a cubic phase with the Pt atom occupying the fcc site and its surrounding six nitrogen atoms form a corner-sharing octahedron [5]. A rotation of the distorted  $\text{PmN}_6$  octahedra results in the marcasite structure for  $\text{OsN}_2$  [9], and yields the baddeleyite ( $\text{CoSb}_2$ ) structure of  $\text{IrN}_2$  [10]. On the basis of a permutation and a combinatorial strategy of the specific sites in the fcc lattice in a 12-atom conventional cell, the thermodynamic stability of all analogues of the aforementioned structures were explored [6], followed by crystal structure prediction using an evolutionary methodology [11]. Despite the fact that several new low-energy layered crystal structures were proposed, only the three classical structures (pyrite, marcasite and baddeleyite) have been experimentally confirmed, and thus structural dependence on the composition motivates us to explore the physical origin of the structural preference for each  $\text{PmN}_2$ .

The stabilization in pyrite-type  $\text{PtN}_2$  was originally attributed to the anchoring effect of strong covalent N-N bonds [1-3,5]. However, it cannot explain the structures of the other pernitrides in view of the fact that the N-N bond lengths (1.40 Å for  $\text{OsN}_2$ , 1.42 Å for  $\text{IrN}_2$ , 1.42 Å for  $\text{PtN}_2$ ) are nearly the same in the various structures. Later on, a Peierls mechanism [12] was proposed to be the origin of the stabilization for the marcasite to baddeleyite transition in  $\text{IrN}_2$  [10]. However, this mechanism cannot elucidate the

stabilization of higher symmetrical structures for OsN<sub>2</sub> and PtN<sub>2</sub> because both the marcasite and pyrite structures are metallic [9]. Therefore, a universal electronic origin of the structural stability has not yet been uncovered.

Since the discovery of the PmN<sub>2</sub> phases their intriguing mechanical properties such as ultrahigh elastic moduli (428 GPa for IrN<sub>2</sub> [3], 358 GPa for OsN<sub>2</sub> [3], and 354 GPa for PtN<sub>2</sub> [1]) and unique electronic structures, e.g., band gaps of  $\sim 2$  eV for PtN<sub>2</sub> [5] and  $\sim 0.4$  eV for IrN<sub>2</sub> [10] have been intensely studied. Moreover, it was proposed that these phases have the potential to be superhard materials [2,3]. By reinforcing the PmN<sub>6</sub> octahedra, the strong covalent N-N bonding was originally thought to result in a strengthening effect in the pernitrides, paving a way for designing strong solids [10,13,14]. However, investigations on transition metal (Tm) nitrides indicate that the weak Tm-N bonds are responsible for the irreversible plastic deformation [15-17], and therefore the strengthening effect of N-N bonds is questionable since the weakest link (e.g., Pm-N and Pm-Pm) would make the lattice instability occur under much lower stress before breaking the N-N bonds [8]. In this letter, a detailed investigation on the anisotropic ideal strengths and atomic deformation paths indicates surprisingly that instead of the strong N-N bonds, the weak Pm-N bonds in the distorted PmN<sub>6</sub> octahedra carry the plastic flow, thereby shedding light on origin of the weakness of PmN<sub>2</sub>.

## II. COMPUTATIONAL METHODS

The present density functional theory (DFT) calculations were performed using the Vienna *Ab-initio* Simulation Package (VASP) [18] with the projector augmented wave (PAW) basis [19] employed to describe the electron-ion interaction and the Perdew,

Burke, and Ernzerhof (PBE) exchange-correlation functional [20] for the exchange correlation term. The kinetic energy cutoff of 600 eV, and the Monkhorst-Pack  $k$ -mesh grids of 8000  $k$ -points per reciprocal atom (KPPRA) [21,22] were adopted for the stress calculations. The phonon dispersions were calculated using the Phonopy code coupled with VASP [23]. Crystal orbital Hamilton populations (COHP) analyses were done using the LOBSTER code [24]. The elastic properties were calculated via the AELAS code [22]. The lattice constants along with the polycrystalline Voigt shear ( $G_V$ ) and bulk ( $B_V$ ) moduli were obtained using the Voigt-Reuss-Hill (VRH) approximation [25,26].

During the calculation of stress-strain relationships under tensile loading, the simulated cell was projected onto a Cartesian coordinate system with one crystallographic direction parallel to a Cartesian axis along which the tension loading was applied. In case of shear deformation, one Cartesian axis was chosen normal to the slip plane and the other Cartesian axis parallel to the slip direction. The simulated cell was incrementally deformed by a transformation of the unstrained cell vector to the strained ones by multiplying the deformation matrices. Afterwards, an ionic relaxation was performed to make both the specific lattice vectors and the ionic coordinates relaxed by fixing the applied strain component while relaxing the other five strain components, until their conjugate stress components, i.e. Hellmann–Feynman stresses, reached less than 0.1 GPa.

Evolutionary structure searches were performed using the open-source evolutionary algorithm (EA) XtalOpt [27,28] along with the default parameter set from Ref. [27]. EA runs were carried out on the Platinum metal (Pm) pernitrides with 2, 3 and 4 formula units in the primitive cell. In this algorithm a new offspring was created as soon as an individual was optimized and the parents were chosen from a population based pool. The

population sizes were around 735, 225, and 110 for the 2, 3 and 4 formula unit cells of the Pm pernitrides, respectively. In each run the same low enthalpy structure was found at least 3 times (often more) before the run was terminated. A four-step structural-optimization scheme was used for all runs, and each step employed the geometry of the structure from the previous step for the initial geometry. Only the ions were allowed to relax in the first step, while the last three steps also allowed the lattice parameters to relax. The precision of the calculation was increased at each step. The calculations were performed using the PBE exchange-correlation functional, the PAW method and an energy cut-off of 500 eV in the final step. The lowest energy structures from each search were optimized using the aforementioned computational settings, to obtain a more accurate energy ranking.

### III. RESULTS AND DISCUSSION

We first searched for the most stable structures of  $\text{PmN}_2$  at 0 GPa and 50 GPa by means of high-throughput screening based on the Inorganic Crystal Structure Database (ICSD) prototype library via the Vienna *Ab-initio* Simulation Package (VASP) code [18]. In total, there are about 300 prototypes with chemical stoichiometry of  $\text{AB}_2$  or  $\text{A}_2\text{B}$  provided in the ICSD [29]. In our work we only considered the 265 structures that have < 35 atoms in the unit cell (the details of the structures are listed in Table S1 [30]). To the best of our knowledge, this is the largest structural prototype library used in high-throughput computations (Note:  $\sim 10$  and  $\sim 100$  prototype structures are considered for  $\text{AB}_2/\text{A}_2\text{B}$  compounds within aflowlib [31] and OQMD [32], respectively). Fig. 1(a)-1(c) shows the calculated formation enthalpies of the 265 prototype structures for  $\text{OsN}_2$ ,  $\text{IrN}_2$

and PtN<sub>2</sub> at 0 GPa and 50 GPa. It is observed that two layered structures have the lowest formation enthalpies for PmN<sub>2</sub> at 0 GPa, including the simple tetragonal (ST) structure belonging to space group 127 (P4/mbm) for PtN<sub>2</sub>, and the simple hexagonal (SH) structure with space group of 191 (P6/mmm) for OsN<sub>2</sub> and IrN<sub>2</sub>. Note that all of these layered structures have also been confirmed by our evolutionary structure searches [27,28]. Although it was proposed that these layered structures could be quenched to atmospheric conditions by phase transformations from structures synthesized under pressure [11,33], all of them are thermodynamically unstable with respect to decomposition into elemental Pm and  $\alpha$ -N<sub>2</sub>, in agreement with the fact that they have not been synthesized so far. At 50 GPa, we found that three high-pressure structures (see Fig. 1(d)-1(f)), including marcasite, baddeleyite and pyrite, are the most stable for OsN<sub>2</sub>, IrN<sub>2</sub> and PtN<sub>2</sub>, respectively. The calculated formation enthalpies for all of the pernitrides are negative (-0.54 eV/atom for OsN<sub>2</sub>, -0.64 eV/atom for IrN<sub>2</sub>, -0.68 eV/atom for PtN<sub>2</sub>), suggesting their thermodynamically feasibility at high pressure. These findings lead to two critical questions: i) Since the formation enthalpies of these pernitrides in the marcasite and baddeleyite structures are comparable, why does OsN<sub>2</sub> adopt the marcasite structure, while IrN<sub>2</sub> prefers the baddeleyite structure? ii) What is the electronic origin of the stabilization of the pyrite structure for PtN<sub>2</sub>?

Before answering these questions, the dynamic stabilities of the three structures are explored by analyzing the high-pressure phonon dispersions (shown in Fig. S1 [30]). A significant soft mode appears at the T (0.5, 0, 0.5) point in marcasite-type IrN<sub>2</sub>, which indicates a cell-doubling phase transition, corresponding to the emergence of the baddeleyite structure, in agreement with a previous report [10]. The basis vectors of the

marcasite structure  $(\vec{a}, \vec{b}, \vec{c})$  correspond to the  $[10\bar{1}]/2$ ,  $[010]$ , and  $[101]/2$  crystal orientations of the baddeleyite structure, respectively. The angle ( $90.51^\circ$  at 50 GPa) between the  $[10\bar{1}]$  and  $[101]$  crystal orientations of the baddeleyite-type  $\text{IrN}_2$  structure has only a small deviation ( $0.51^\circ$ ) from the corresponding angle in the marcasite structure. Both baddeleyite-type and marcasite-type  $\text{OsN}_2$  are dynamically stable, whereas the acoustic branches of the latter have larger slopes around the  $\Gamma$  point, suggesting a larger elastic stiffness. For  $\text{PtN}_2$ , the absence of imaginary modes indicates the dynamic stabilities of the baddeleyite, marcasite, and pyrite structures, while pyrite-type  $\text{PtN}_2$  is favored because of its lowest formation enthalpy.

To investigate the relative stabilities of  $\text{OsN}_2$  and  $\text{IrN}_2$  in different structure types at 50 GPa more clearly, hypothetical structures containing elements from the left hand side of the periodic table  $\text{WN}_2$ ,  $\text{ReN}_2$ , and right hand side of the periodic table  $\text{AuN}_2$ ,  $\text{HgN}_2$  with three structure types have also been included for comparison. Besides the formation enthalpy,  $\Delta H$ , we have considered the PV term in enthalpy,  $PV$ , and the N-N bond length,  $d_{\text{N-N}}$ , as additional descriptors (see Fig. 2(a)). Similar to  $\text{IrN}_2$ , both  $\text{WN}_2$  and  $\text{ReN}_2$  with baddeleyite-type structures have the lowest  $\Delta H$  among the three structure types. The too positive  $\Delta H$  makes it unlikely that the three phases of  $\text{AuN}_2$  and  $\text{HgN}_2$  will be synthesized experimentally [34]. The enthalpy,  $H$ , is defined as  $H = U + PV$ , where  $U$ ,  $P$ , and  $V$  are the internal energy, pressure, and volume per formula unit, respectively. Interestingly, the most stable structure was found to have the lowest  $PV$  contribution to  $H$  for each pernitride, except for baddeleyite-type  $\text{IrN}_2$  and  $\text{HgN}_2$ , where the preferred structure was stabilized via the  $U$  term. Turning to  $d_{\text{N-N}}$ , it may be noticed that  $d_{\text{N-N}}$  can be divided into two regions: the first five compounds (i.e.,  $\text{WN}_2$ - $\text{PtN}_2$ ) have values that are

closer to that of an N-N single bond (1.45 Å); while the latter two (i.e., AuN<sub>2</sub> and HgN<sub>2</sub>) are closer to an N-N double bond (1.25 Å). Since all three structures of AuN<sub>2</sub> and HgN<sub>2</sub> are unstable, we focus on the first five compounds (i.e., WN<sub>2</sub>-PtN<sub>2</sub>). The formal oxidation states of the elements within these PmN<sub>2</sub> can be considered to be Pm<sup>4+</sup> and N<sub>2</sub><sup>4-</sup> (see Fig. 3(a)) [13]. More impressively, the fluctuation of  $d_{\text{N-N}}$  correlates with an even/odd  $d$ -electron configuration in marcasite-type WN<sub>2</sub> ( $d^2$ ), ReN<sub>2</sub> ( $d^3$ ), OsN<sub>2</sub> ( $d^4$ ), IrN<sub>2</sub> ( $d^5$ ), and PtN<sub>2</sub> ( $d^6$ ). It might be attributed to the fact that fewer  $d$  electrons are donated to N, which results in filling an antibonding level, when Pm<sup>4+</sup> possesses an odd number of  $d$  electrons ( $d^3$  and  $d^5$ ) as opposed to an even number ( $d^2$ ,  $d^4$  and  $d^6$ ), to maintain the symmetry of the degenerate electronic state of Pm<sup>4+</sup>. Considering the aforementioned soft phonon mode in marcasite-type IrN<sub>2</sub> that leads to the marcasite-baddeleyite transition, it may be surprising that less electrons are donated to N<sub>2</sub> in this phase.

To solve this puzzle, Crystal Orbital Hamiltonian Population (COHP) and Electronic Localization Function (ELF) analyses were performed and the results are shown in Fig. 2(b)-2(c) and Fig. S2 [30], respectively. It is seen in combination with Fig. 3(b) that the distortion leading to the marcasite-baddeleyite transition leads to Pm dimerization [10], which brings a sharp increase of the Pm-Pm integrated -COHP (see the orange areas in Fig. 2(b)-2(c) and Table S2 [30]), and a distinctly delocalized electron distribution between Pm pairs in the ELF maps in baddeleyite-type OsN<sub>2</sub> and IrN<sub>2</sub>. This indicates that the Pm-Pm bonding gradually weakens in going from OsN<sub>2</sub> and IrN<sub>2</sub> as the  $d$ -electron count increases, yet it is not observed in PtN<sub>2</sub>. Pm dimerization results in a broadened  $d_{xy}$  band and narrowed  $d_{x^2-y^2}$  band, as shown in Fig. 3(b), which can be used to quantify the extent of bonding and antibonding, respectively. Since the structural distortion has

negligible effect on the other d states, marcasite-type  $\text{OsN}_2$  and baddeleyite-type  $\text{IrN}_2$  are preferred due to the maximized filling of bonding ( $d_{xy}$ ) and minimal filling of the antibonding ( $d_{x^2-y^2}$ ) states, which lead to the anchoring effect of distorted octahedra. Whereas the Pm-N bond strength in these two structures is similar, as shown by the integrated  $-\text{COHP}$ , the N-N bond strength is not. Pm dimerization results in a larger donation of electrons to the antibonding states in N-N, thereby leading to an increased N-N bond length [13], as illustrated in Fig. 2(a) and Table S2 [30]. For baddeleyite-type  $\text{OsN}_2$ , a larger filling of the N-N antibonding states leads to a large density of states (DOS) at the Fermi level, which is typically a characteristic of unstable structures; whereas in marcasite-type  $\text{IrN}_2$ , a few electrons fill the N-N antibonding states, leaving a finite value near the Fermi level, thereby opening up a band gap [10]. In brief, N-N electron filling plays a destabilizing role in baddeleyite-type  $\text{OsN}_2$  and marcasite-type  $\text{IrN}_2$ .

To understand the stabilization of  $\text{PtN}_2$  in the pyrite structure at 50 GPa, ELF and COHP analyses were carried out. The results indicated that the Pm-Pm bonding induced by Pm dimerization in all three structures is weak and can be neglected (shown in Fig. S2 and Table S2 [30]). Although all three structures of  $\text{PtN}_2$  are semiconductors (see Fig. S3 [30]), the largest band gap appears in the pyrite structure, suggesting that the hybridization between the Pm-d and N-p states is strongest in this structure. This indicates that the Pm-N bonding interaction plays a moderate role in the stabilization of pyrite-type  $\text{PtN}_2$ .

We next explore the elasticity and mechanical strengths of the most stable structures of  $\text{IrN}_2$ ,  $\text{OsN}_2$  and  $\text{PtN}_2$  to determine if they may possess superior mechanical properties.

Table 1 lists the calculated elastic properties of the pernitrides and several well-known hard/superhard materials [5,8,9,14,35-39]. It is seen that the three pernitrides show comparable bulk and shear moduli to those of superhard c-BN and ultra-incompressible ReB<sub>2</sub>, indicating their ultra-incompressibility and high stiffness. According to the hardness model [40] based on elastic moduli  $G$  and Pugh's ratio  $k$  [41], i.e.,  $H_v = 2(k^2G)^{0.585} - 3$ , OsN<sub>2</sub> is found to possess the highest bulk modulus (369 GPa) and hardness (27.1 GPa) among the three nitrides. However, it is generally accepted that plasticity descriptors should be included to get a more realistic quantification of plastic resistance or hardness [42]. Therefore, the ideal strength is evaluated. Table 1 lists the determined minimum ideal tensile and shear strengths along the weakest deformation path. Interestingly, the ideal shear strengths of the three pernitrides follow the trends of the hardness models; OsN<sub>2</sub> (25.7 GPa) possess the highest shear strength, which is followed by PtN<sub>2</sub> (25.6 GPa) and IrN<sub>2</sub> (21.6 GPa). All these values are much lower than those of hard ReB<sub>2</sub> (32.9 GPa) and superhard c-BN (55.3 GPa), ruling them out from the intrinsic superhard materials.

We finally explored the atomic deformation mechanism and electronic origin that intrinsically limits the mechanical strengths of the three pernitrides. Taking IrN<sub>2</sub> as an example, Fig. 4 illustrates the stress-strain curves and variation of Pm-N bond length during straining along the weakest deformation path. It is unexpected that the lattice instability originates from the breaking of the Pm-N bonds that elongate in the PmN<sub>6</sub> octahedra along specific shear deformation paths. Interestingly, no structural transformation is observed before approaching the critical strain, yet an anomalous variation appears for Pm-N bond lengths and stress. A similar creep-like behavior was

observed in  $\text{WB}_4$  under straining [43]. The loading process can be divided into four stages:  $S_0$ - $S_1$ ,  $S_1$ - $S_2$ ,  $S_2$ - $S_3$ , and  $S_3$ - $S_4$ , where  $S_0$ ,  $S_1$ ,  $S_2$ ,  $S_3$ , and  $S_4$  represent the equilibrium state, local stress maximum state, local stress minimum state, critical strain state, and lattice instability state, respectively. Noticeably, the transition point of anomalous change of the Ir-N1 distance,  $d_{\text{Ir-N1}}$ , begins exactly at  $S_1$ . Between  $S_1$ - $S_2$  both the stress and  $d_{\text{Ir-N1}}$  decrease, then they increase during the  $S_2$ - $S_3$  stage. Almost the opposite trend is observed for  $d_{\text{Ir-N2}}$ . This suggests that the  $\text{PmN}_6$  octahedron rotates at the  $S_1$ - $S_3$  stage (a schematic is shown in Fig. 3(c)), which affects the Pm-N bond lengths and redistributes charge. The latter can be identified by the deformed valence charge-density differences (VCDD), as shown in Fig. 4. A positive (yellow color) or negative (cyan color) value indicates an accumulation (bond strengthening) or depletion (bond weakening) of charge, respectively. At  $S_1$ , the longer Ir-N1 bond has a stronger directional (covalent) charge distribution as compared to that of Ir-N2, which is accompanied by a strain-induced metal-semimetal transition revealed by the deformed electronic structure analysis (see the lower panel for  $S_1$  in Fig. 4). The bands composed of Pm-Pm antibonding states (see Fig. 2(b) and 3(b)) and a few N-p states (see the red circle in Fig. 4) move below the Fermi level along the high symmetry line joining the  $\Gamma$ -Y points. The charge distribution between the Ir-N2 bonds shows an increasing directionality, and a semimetal-metal transition occurs as the strain increases at  $S_1$ - $S_3$ . The bond length and charge distribution of Ir-N1 and Ir-N2 become similar at  $S_2$ - $S_3$ . The narrow bands become dispersed with an increasing N-p state. From  $S_3$  to  $S_4$ , the lattice is destabilized and the N-N bond length decreases sharply (1.36 to 1.27 Å), suggesting the formation of N-N double bonds at  $S_4$ . A similar anomalous variation appears for Os-N2

bond lengths and stress in OsN<sub>2</sub>, while a metallic character remains during straining (see Fig. S4 [30]). Although a similar semiconductor-semimetal-metal transition also appears in PtN<sub>2</sub>, a monotonic stress change and smaller critical strain suggest the brittle nature (see Fig. S5 [30]). In brief, the anchoring effect of distorted octahedra is responsible for the weakness of the pernitrides, in similar manner to the role of Tm-N bonding widely observed in TmNs [15-17].

#### IV. CONCLUSIONS

In summary, two long-standing critical questions related to the stabilization of specific space groups and mechanical strengths for the platinum metal pernitrides are studied by using high-throughput screening and evolutionary algorithms, orbital-resolved electronic structure analyses and ideal strength calculations. Our results suggest that the stabilization of these pernitrides at high pressure cannot be simply understood by considering N-N bonding and Peierls distortions, but instead can be quantified by the anchoring effect of distorted PmN<sub>6</sub> octahedra via an orbital-resolved combinatorial strategy, which maximizes the stabilization (destabilization) effects derived from specific bonding (antibonding) interactions in specific crystal structures. The calculated plastic resistance and failure mechanism have unexpectedly ruled PmN<sub>2</sub> out of the intrinsically superhard materials because the weak Pm-N bonds in the distorted PmN<sub>6</sub> octahedra cause an electronic instability and plastic flow. These findings clarify the physical origin of high-pressure stabilization of PmN<sub>2</sub> and highlight the necessity to explore atomic deformation mechanism in the design of novel strong solids.

## ACKNOWLEDGEMENTS

This work is supported by the National Key Research and Development Program of China (No. 2016YFC1102500) and National Natural Science Foundation of China (NFSC) with No. 51672015, and National Thousand Young Talents Program of China. D. L. acknowledges support by the European Regional Development Fund in the IT4Innovations national supercomputing center – Path to Exascale project, No. CZ.02.1.01/0.0/0.0/16\_013/0001791 within the Operational Programme Research, Development and Education and by the Ministry of Education by Czech Science Foundation project No. 17-27790S, and grant No. 8J18DE004 of Ministry of Education, Youth, and Sport of the Czech Republic. E.Z. acknowledges the NSF (DMR-1505817) for financial support. We would also like to thank Prof. G. Kresse for valuable advice for the application of VASP.

## REFERENCES

- [1] E. Gregoryanz, C. Sanloup, M. Somayazulu, J. Badro, G. Fiquet, H.-k. Mao, and R. J. Hemley, *Nat. Mater.* **3**, 294 (2004).
- [2] J. C. Crowhurst, A. F. Goncharov, B. Sadigh, C. L. Evans, P. G. Morrall, J. L. Ferreira, and A. J. Nelson, *Science* **311**, 1275 (2006).
- [3] A. F. Young, C. Sanloup, E. Gregoryanz, S. Scandolo, R. J. Hemley, and H.-k. Mao, *Phys. Rev. Lett.* **96**, 155501 (2006).
- [4] J. C. Crowhurst, A. F. Goncharov, B. Sadigh, J. M. Zaug, D. Aberg, Y. Meng, and V. B. Prakapenka, *J. Mater. Res.* **23**, 1 (2011).
- [5] A. F. Young, J. A. Montoya, C. Sanloup, M. Lazzeri, E. Gregoryanz, and S. Scandolo, *Phys. Rev. B* **73**, 153102 (2006).
- [6] D. Åberg, B. Sadigh, J. Crowhurst, and A. F. Goncharov, *Phys. Rev. Lett.* **100**, 095501 (2008).
- [7] Z. T. Y. Liu, D. Gall, and S. V. Khare, *Phys. Rev. B* **90**, 134102 (2014).
- [8] R. F. Zhang, D. Legut, Z. H. Fu, S. Veprek, Q. F. Zhang, and H. K. Mao, *Phys. Rev. B* **92**, 104107 (2015).
- [9] J. A. Montoya, A. D. Hernandez, C. Sanloup, E. Gregoryanz, and S. Scandolo, *Appl. Phys. Lett.* **90**, 011909 (2007).
- [10] R. Yu, Q. Zhan, and L. C. De Jonghe, *Angew. Chem. Int. Ed.* **46**, 1136 (2007).
- [11] C. Z. Fan, J. Li, M. Hu, Z. S. Zhao, B. Xu, and J. L. He, *J. Superhard Mater.* **35**, 339 (2013).
- [12] R. E. Peierls, *Quantum theory of solids* (Oxford University Press, 1955).
- [13] M. Wessel and R. Dronskowski, *J. Am. Chem. Soc.* **132**, 2421 (2010).
- [14] Z.-j. Wu, E.-j. Zhao, H.-p. Xiang, X.-f. Hao, X.-j. Liu, and J. Meng, *Phys. Rev. B* **76**, 054115 (2007).
- [15] R. F. Zhang, S. H. Sheng, and S. Veprek, *Appl. Phys. Lett.* **94**, 121903 (2009).
- [16] R. F. Zhang, Z. J. Lin, H.-K. Mao, and Y. Zhao, *Phys. Rev. B* **83**, 060101 (2011).
- [17] R. F. Zhang, S. H. Sheng, and S. Veprek, *Scr. Mater.* **68**, 913 (2013).
- [18] G. Kresse and J. Furthmüller, *Comput. Mater. Sci.* **6**, 15 (1996).
- [19] P. E. Blöchl, *Phys. Rev. B* **50**, 17953 (1994).
- [20] J. P. Perdew, K. Burke, and M. Ernzerhof, *Phys. Rev. Lett.* **77**, 3865 (1996).
- [21] A. van de Walle and G. Ceder, *J. Phase Equilib.* **23**, 348 (2002).
- [22] S. H. Zhang and R. F. Zhang, *Comput. Phys. Commun.* **220**, 403 (2017).
- [23] A. Togo, F. Oba, and I. Tanaka, *Phys. Rev. B* **78**, 134106 (2008).
- [24] R. Dronskowski and P. E. Bloechl, *J. Phys. Chem.* **97**, 8617 (1993).
- [25] R. Hill, *The Elastic Behaviour of a Crystalline Aggregate* 1952), Vol. 65, *Proc. Phys. Soc. London*, Sect. A, 5.
- [26] R. Hill, *J. Mech. Phys. Solids* **11**, 357 (1963).
- [27] D. C. Lonie and E. Zurek, *Comput. Phys. Commun.* **182**, 372 (2011).
- [28] D. C. Lonie and E. Zurek, *Comput. Phys. Commun.* **182**, 2305 (2011).

- [29] A. Belsky, M. Hellenbrandt, V. L. Karen, and P. Luksch, *Acta Cryst. B* **58**, 364 (2002).
- [30] See Supplemental Material at <https://journals.aps.org/prmaterials/> for ICSD prototype library, calculated -COHP integrated to the Fermi level, high-pressure phonon dispersions, and ELF maps of PmN<sub>2</sub>; Calculated PDOS and COHP curves of PtN<sub>2</sub>, The calculated stress and bond length vs strain curves of OsN<sub>2</sub> and IrN<sub>2</sub>.
- [31] S. Curtarolo, W. Setyawan, S. Wang, J. Xue, K. Yang, R. H. Taylor, L. J. Nelson, G. L. W. Hart, S. Sanvito, M. Buongiorno-Nardelli *et al.*, *Comput. Mater. Sci.* **58**, 227 (2012).
- [32] J. E. Saal, S. Kirklin, M. Aykol, B. Meredig, and C. Wolverton, *JOM* **65**, 1501 (2013).
- [33] Z. H. Wang, X. Y. Kuang, M. M. Zhong, P. Lu, A. J. Mao, and X. F. Huang, *Europhys. Lett.* **95**, 66005 (2011).
- [34] W. Chen, J. S. Tse, and J. Z. Jiang, *Solid State Commun.* **150**, 181 (2010).
- [35] R. F. Zhang, S. Veprek, and A. S. Argon, *Appl. Phys. Lett.* **91**, 201914 (2007).
- [36] R. F. Zhang, S. Veprek, and A. S. Argon, *Phys. Rev. B* **77**, 172103 (2008).
- [37] R. F. Zhang, Z. J. Lin, and S. Veprek, *Phys. Rev. B* **83**, 155452 (2011).
- [38] H. Bu, M. Zhao, Y. Xi, X. Wang, H. Peng, C. Wang, and X. Liu, *Europhys. Lett.* **100**, 56003 (2012).
- [39] A. Nagakubo, H. Ogi, H. Sumiya, K. Kusakabe, and M. Hirao, *Appl. Phys. Lett.* **102**, 241909 (2013).
- [40] X. Q. Chen, H. Y. Niu, D. Z. Li, and Y. Y. Li, *Intermetallics* **19**, 1275 (2011).
- [41] S. F. Pugh, *Philos. Mag.* **45**, 823 (1954).
- [42] S. Veprek, *J. Vac. Sci. Technol. A* **31**, 050822 (2013).
- [43] Q. Li, D. Zhou, W. Zheng, Y. Ma, and C. Chen, *Phys. Rev. Lett.* **115**, 185502 (2015).

**Table 1.** Calculated Voigt polycrystalline bulk ( $B_V$ ) and shear ( $G_V$ ) moduli, Pugh ratio  $k$  [41], as well as calculated minimum ideal tensile ( $\sigma_{\min}$ ) and shearing ( $\tau_{\min}$ ) strength. The “Vickers hardness” ( $H_V^{\text{Chen}}$ ) is provided according to the Chen et al. empirical hardness model [40].

	$B_V/\text{GPa}$	$G_V/\text{GPa}$	$k$	$H_V^{\text{Chen}}/\text{GPa}$	Tension direction	$\sigma_{\min}/\text{GPa}$	Shear direction	$\tau_{\min}/\text{GPa}$	Ref.
Diamond	437	542	1.24	99.3	$\langle 111 \rangle$	82.3	$(111)\langle 11\bar{2} \rangle$	86.8	[37,38]
c-BN	372	381	1.02	63.5	$\langle 111 \rangle$	55.3	$(111)\langle 11\bar{2} \rangle$	58.3	[36]
ReB <sub>2</sub>	348	274	0.79	37.3	$\langle \bar{1}2\bar{1}0 \rangle$	58.5	$(0001)\langle 10\bar{1}0 \rangle$	32.9	[35]
OsN <sub>2</sub>	369	241	0.65	27.1	$\langle 101 \rangle$	42.1	$(010)\langle 101 \rangle$	25.7	this work
	359								[9]
IrN <sub>2</sub>	342	221	0.65	25.2	$\langle 101 \rangle$	26.1	$(001)\langle 100 \rangle$	21.6	this work
	354	224	0.63	24.8					[14]
PtN <sub>2</sub>	286	203	0.71	27.0	$\langle 100 \rangle$	28.4	$(111)\langle \bar{1}\bar{1}2 \rangle$	25.6	this work
	288	221	0.77	31.5					[5]
	286	203	0.71	27.0	$\langle 100 \rangle$	28.5	$(111)\langle \bar{1}\bar{1}2 \rangle$	25.5	[8]

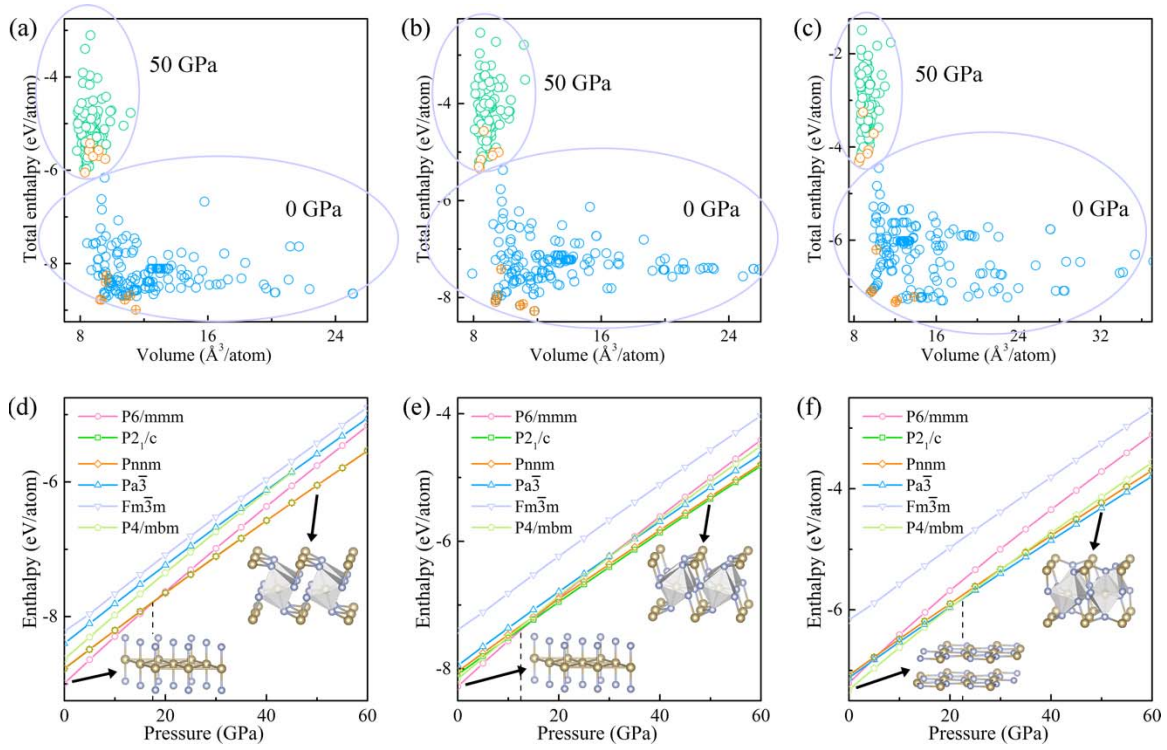


**Fig. 1.** The high-throughput screening of the most stable structures of (a) OsN<sub>2</sub>, (b) IrN<sub>2</sub> and (c) PtN<sub>2</sub> according to the 265 crystallographic structure prototypes collected in the ICSD library. The enthalpy-pressure relationships of (d) OsN<sub>2</sub>, (e) IrN<sub>2</sub> and (f) PtN<sub>2</sub> in six select structures, i.e., simple hexagonal (P6/mmm), baddeleyite (P2<sub>1</sub>/c), marcasite (Pnmm), pyrite (Pa-3), face-centered cubic (Fm-3m), and simple tetragonal (P4/mbm) are provided.

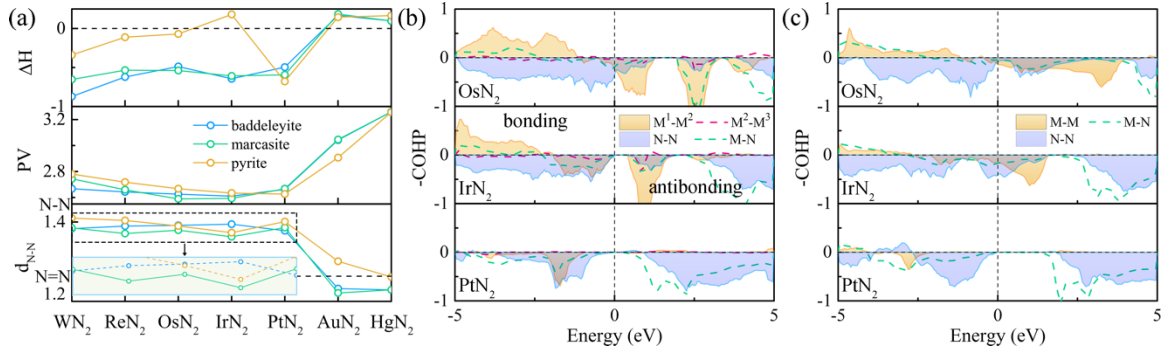


**Fig. 2.** (a) Calculated formation enthalpies  $\Delta H$  (Unit: eV/atom), PV term  $PV$  (Unit: eV/atom), and bond lengths  $d_{N-N}$  (Unit: Å) of N-N pairs as a function of the transition metal in pernitrides assuming the baddeleyite, marcasite, and pyrite structures at 50 GPa. The inset shows an enlarged view for  $WN_2$ - $PtN_2$ . Calculated -COHP curves of (b) baddeleyite and (c) marcasite structures of  $OsN_2$ ,  $IrN_2$  and  $PtN_2$ .

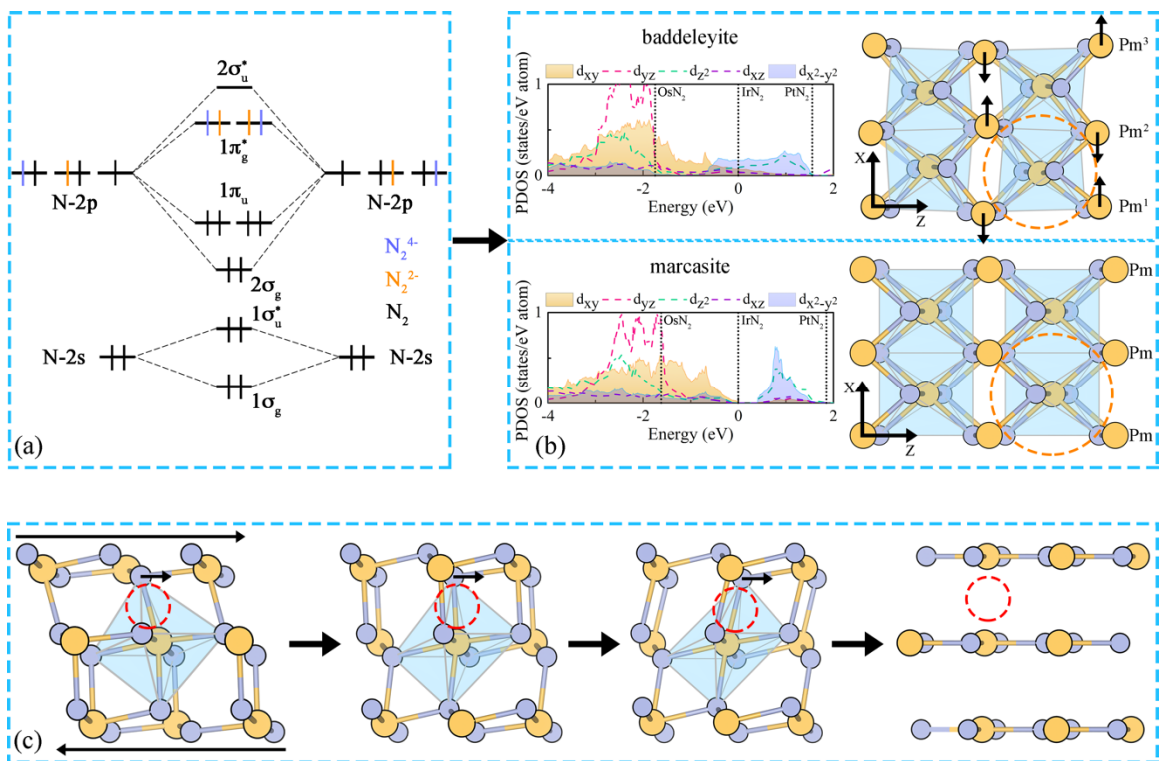


**Fig. 3.** (a) Qualitative molecular-orbital (MO) diagram of N<sub>2</sub> with different degrees of electron filling. (b) A comparison of a structural distortion diagram and partial density of states (PDOS) of baddeleyite- and marcasite-type structure. (c) An illustration of structural evolution of IrN<sub>2</sub> under shear strain along the weakest path.

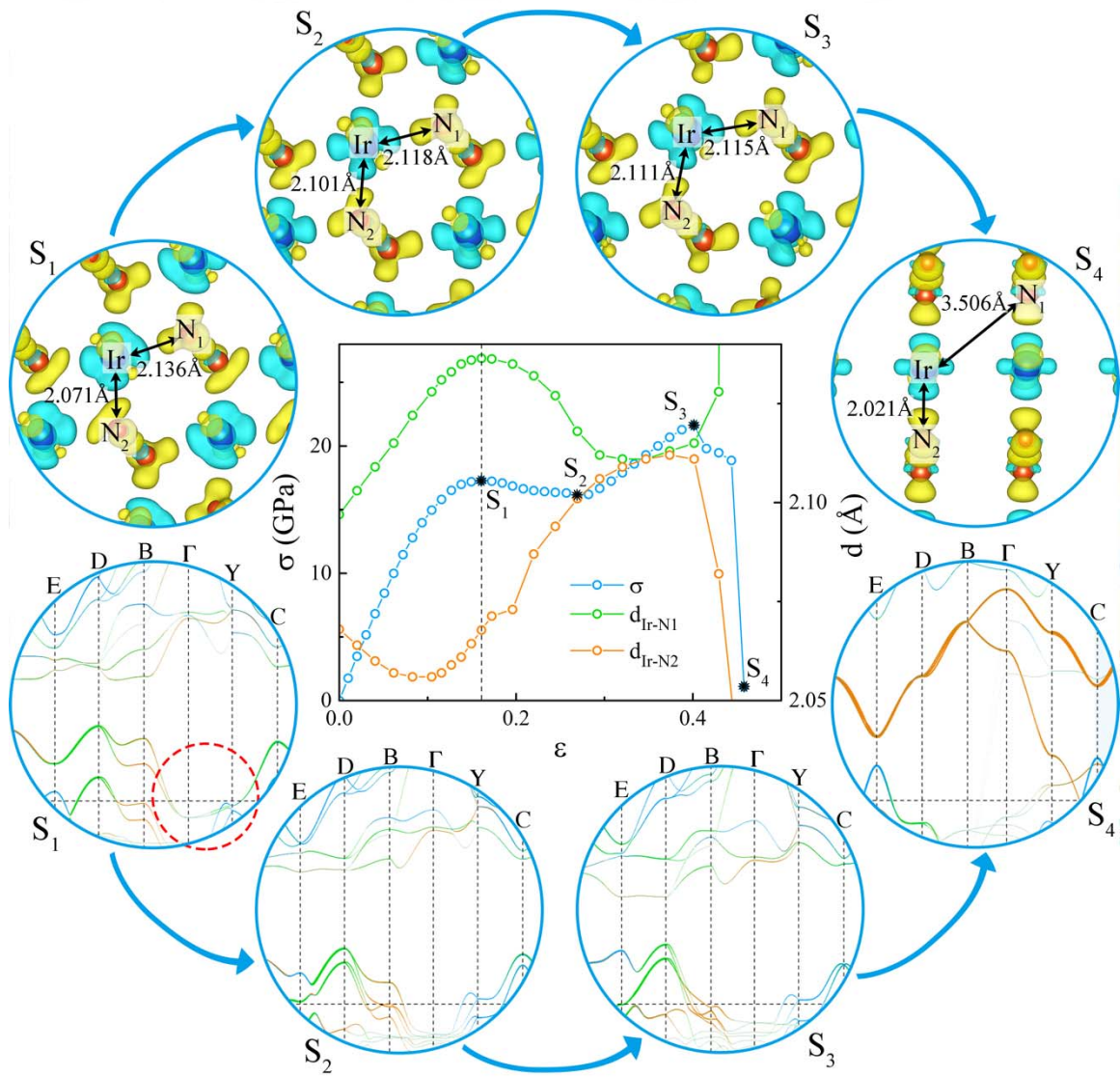


**Fig. 4.** The calculated stress  $\sigma$  and bond length  $d_{\text{Ir-N}}$  vs strain  $\epsilon$  curves of IrN<sub>2</sub> along the weakest shearing path. We selected four snapshots of the deformed orbital-resolved band structures and the valence charge-density differences (VCDD) under different shear strains to reveal the electronic origin. The orange, blue, and green colors represent three p orbitals of N, respectively. The isosurface of the VCDD correspond to  $\pm 0.022 e/\text{Bohr}^3$ .